Pham Van Tien · Kyoji Sassa · Kaoru Takara · Hiroshi Fukuoka · Khang Dang · Tatsuya Shibasaki · Nguyen Duc Ha · Hendy Setiawan · Doan Huy Loi

# Formation process of two massive dams following rainfall-induced deep-seated rapid landslide failures in the Kii Peninsula of Japan

**Abstract** Extreme heavy rainfall due to Typhoon Talas on September 2–4, 2011 in the Kii Peninsula, Japan, triggered numerous floods and landslides. This study investigates the mechanism and the entire process of rainfall-induced deep-seated landslides forming two massive dams in the Kuridaira and Akatani valleys, respectively. The mechanism of the rapid deep-seated landslides is examined through a series of laboratory experiments on samples from sliding surfaces by using undrained high-stress dynamic-loading ring-shear apparatus. The test results indicate that the failure of samples is triggered by excess pore water pressure generation under a shear displacement from 2 to 7 mm with a pore pressure ratio ranging from 0.33 to 0.37. The rapid movement of landslides is mainly attributed to high mobility due to the liquefaction behavior of both sandstone-rich and shale samples. Geomorphic settings and landslide mobility are major contributing factors to the dam formation. Additionally, shear displacement control tests show that a certain amount of shear displacement between 2 and 7 mm along the sliding surfaces of the gravitationally deformed slopes might have led to the failures. Importantly, computer simulation with LS-RAPID software using input parameters obtained from physical experiments is employed to interpret the entire formation process of the abovementioned two landslide dams. The simulation results are examined in accordance with the observed on-site geomorphic features and recorded data to explain the possibility of sliding processes. The results further point out that local failures are initiated from the lower middle part of the landslide bodies where the geological boundary exists. This condition most probably influences the landslide initiation in the two case studies. This research is therefore helpful for hazard assessment of slopes that are susceptible to deep-seated landslides and other sequential processes in areas with geology and geomorphology similar to that of the Kii Peninsula.

**Keywords** Deep-seated rapid landslide · Landslide dam · Rainfall · Ring-shear apparatus · LS-RAPID · Kuridaira · Akatani · Kii Peninsula

## Introduction

Geomorphic processes like landslides lead to the formation and development of a valley landscape, such as the formation of a catchment, alluvial fan, or debris fan, channel constriction, and temporary or permanent stream blockage (Korup 2002). Downslope movements resulting in the obstruction of river valleys can induce secondary hazards when landslide dams form and fail (Costa and Schuster 1987). The resulting destruction occurs with the rapid movement of landslides and the subsequent impacts of the landslide-formed dams, including dam breach, upstream inundation, and downstream flooding (Korup 2005). Therefore, it is important to ascertain the sliding mechanism and to study the possibility of landslide dam formation for hazard assessment of sequent events and scenario planning to the ends of disaster prevention and preparedness.

There are many reports on deep-seated landslides and the aftermath of dam formations worldwide, e.g., the Hattian Bala landslide in Pakistan (Dunning et al. 2007), the catastrophic Shiaolin landslide in Taiwan (Tsou et al. 2011), more than 50 large landslides triggered by the M6.8 Mid-Niigata Prefecture Earthquake (Sassa 2005) and the 17 rainfall-induced deep-seated landslides in the Kii Peninsula (SABO 2013) in Japan, the giant Daguangbao landslide in China (Huang et al. 2012), and the Sunkoshi landslide in Nepal (MOI 2014). The mechanisms of deep-seated landslides have been widely investigated through geological and morphological features (Geertsema et al. 2006; Chigira 2011 and 2014; Chigira et al. 2013; Miyagi et al. 2011) or geotechnical simulations (Petley and Allison 1997; Kilburn and Petley 2003; Sassa et al. 2010, 2014; Setiawan, 2017). The possibility and conditions of landslide dam formation have also been well-studied via geomorphological parameters (Costa and Schuster 1987; Evans 2006; Chen et al. 2016; Ermini et al. 2006; Stefanelli et al. 2017). These indexes usually combine two or more morphological parameters to characterize the landslides (e.g., the volume, depth, velocity of mass movement) and the river valley (e.g., catchment area, valley width, slope parameters). In addition, much research has focused on the susceptibility of landslide dams to failure and their cascading effects (Costa and Schuster 1987; Korup 2002 and 2005; Ermini and Casagli 2003; Peng and Zhang 2012; Fan et al. 2012). However, these studies of landslide dams have mostly been descriptive and focused on the hazard assessment of consequential effects. They traditionally consider the issues of landslides and dam formation separately (Korup 2002). Therefore, research that incorporates landslide initiation and motion into the formation process of dams is indispensable for a comprehensive understanding of landslide dams. Together with the analysis of morphological indexes, research on the physical mechanism by which landslide dams are formed is needed, since landslide initiation and its post-failure motion significantly influence dam formation.

This paper thus aims to investigate the physical mechanism and geotechnical factors controlling the landslide dam formation and to present its formation process through the typical cases of the two massive dams formed by the Kuridaira and Akatani deep-seated landslides that occurred during the 2011 heavy rainfall event in the Kii Peninsula, Japan in 2011. To do this, a site study, laboratory tests, and computer modeling were carried out. The entire process of rainfall-induced deep-seated landslides that results in the dam formation is analyzed by a computer simulation done with the LS-RAPID software. The simulation recreates the

event by integrating the physical soil parameters measured in high-stress dynamic-loading ring-shear tests. Geotechnical tests and the computer simulation provide a comprehensive insight into the physical mechanisms and entire formation process of landslide dams which has not been adequately addressed in the previous studies. Otherwise, parameters, including the depth, volume, extent, and physical properties of constituent materials of the landslide dams, obtained from the ring-shear and computer simulations are useful inputs for simulating other sequential effects such as dam breaching and flooding. Hazard assessment of the formation and failure of landslide dams, as showcased in this study, is therefore adequate for disaster mitigation and preparedness in upstream and downstream areas, particularly in the Kii Peninsula which frequently suffers from a number of large-scale deep-seated landslides and landslide dams in rainy seasons.

## Case studies

The Kii Peninsula, located in the Cretaceous to Neogene Shimanto accretional complex in the southeast of Japan (GSJ 1998, Fig. 1a, b), is known as regions prone to frequent deep-seated catastrophic landslides (Hayashi et al. 2013). In September 2011, the Kii Peninsula of Japan suffered an extensive landslide disaster triggered by record-breaking rainfall brought by Typhoon Talas. This event triggered more than 3000 landslides, covering about 100 million m³ of landslide sediments, where large-scale deep-seated landslides exceeding 1 ha were found in 72 locations, forming a total of 17 massive landslide dams. After the disaster, the five largest landslide dams, namely Kuridaira, Akatani, Nagatono, Kitamata, and Iya, still exist and were identified by the Ministry of Land, Infrastructure, Transport and Tourism for urgent countermeasures against secondary hazards from overflow, debris flow, erosion, and dam breach (Hayashi et al. 2013; SABO 2013). The case studies for this study were the two largest deep-seated landslide dams in Kuridaira and Akatani valleys, respectively, in Totsukawa village, Yoshino district, and in Gojo city of Nara prefecture (Fig. 1c, d). These landslide dams were selected because of their typical features in terms of geology, topography, triggering factors, and failure characteristics for this area. Landslides in both valleys were preceded by pre-existing small scarps near the heads of the gravitational deformation slopes (Chigira et al. 2013).

The landslides were induced by cumulative precipitation exceeding 1800 mm between August 31 and September 4 at Kamikitayama AMeDAS Station, 17 km northeast of the Kuridaira slope (Fig. 2). Typhoon Talas produced a maximum 72-h rainfall of 1650.5 mm and a maximum daily rainfall of 661 mm on September 3. The cumulative precipitation that triggered the Kuridaira and Akatani landslides were approximately 1516.5 and 1746 mm, respectively. The Kuridaira landslide occurred at 23:06:13 on September 3, with a duration of 100 s, and the Akatani landslide occurred at 7:22:00 on September 4 over 70 s (Yamada et al. 2012). After the 2011 event, large-scale debris flows severely occurred from the upper part of the Akatani landslide during the rainstorm seasons between 2012 and 2014 (SABO 2014b). Morphological features of the Akatani landslide area are presented in Fig. 3. Landslide deposits consist of rock debris of mudstone-rich materials and sandstone-rich materials and its fragments. Chigira et al. (2013) estimated the maximum velocity of the movement of the Akatani landslide as ranging from 80 to 100 km/h.

The massive movement of the Kuridaira and Akatani landslides blocked the valley courses and formed 100- and 85-m-high natural dams in catchment areas of 8.7 and 13.2 km², respectively (SABO 2013). The Kuridaira landslide had the largest volume (23.0 million m³) and was about 100 m deep, 800 m long, and 600 m wide. The Akatani landslide had a volume of 10.2 million m³ with a depth of 67 m, length of 1000 m, and width ranging from 300 m at the head to 500 m at the toe. These dimensions were calculated from 5-m digital elevation model (DEM) data in September 2011 (SABO 2015). The geological plan and profile of the two slopes after sliding are shown in Fig. 4. The Kuridaira slope exposed interbedded sandstone and shale, shale- or sandstone-dominated alternation rocks, and clastic deposits (Fig. 4a, c), whereas the Akatani slope consists of interbedded rocks of sandstone, sandstone- or mudstone-rich materials, and landslide debris above its sliding plane (Fig. 4b,d). Both sliding directions were mainly the dip direction of the strata along northwest dip-slip faults of interbedded broken formations and mixed sedimentary rocks. The sliding surface of the Kuridaira landslide was predominantly formed on the alternating layers of shale and sandstone-dominated rocks, whereas the Akatani landslide mostly moved down along the layer of sandstone-rich rocks. Geological features of the landslides with structures of mixed rocks, broken formations, and wedge-shaped discontinuities create conditions favorable for the build-up of the groundwater table (Chigira et al. 2013).

The 2011 disaster attracted much attention and subsequently motivated scientists and engineers to examine the geological and topographical features of landslides and to make risk assessments of secondary hazards (Chigira et al. 2013; Kojima et al. 2016; SABO, 2013, SABO, 2014a, b; Wang et al. 2014). However, most of these studies looked mainly at certain aspects of landslide dams in isolation, instead of studying deep-seated landslides coupled with dam formation as a process. In addition, the mechanism and process of deep-seated rapid landslides in the Kii Peninsula remain poorly understood (Tien et al. 2018). There is hence an acute need to conduct a computer simulation that employs the physical parameters from laboratory experiments to reproduce the processes behind dam-forming landslides. This study, therefore, attempts to answer two important questions regarding the mechanisms of dam-forming landslides and how massive movements formed two specific landslide dams in the Kii Peninsula: first, what are the formation mechanisms of natural landslide dams induced by rainfall and the factors that govern rapid-moving landslides in accretionary sedimentary zones with the alternation of mudstone, sandstone, shale, and greenstone? Second, what are the initiation and motion behavior in the entire process of two specific landslide dams, including the onset of failures, the sequence of block movement, the behavior of subsequent debris flow, and the landslide dam formation?

## Method

Two questions that have been raised in this paper are as follows: What are the mechanisms of the two rapid landslides forming natural dams and how the dams were formed in the river valleys. Ring shear tests (Sassa et al. 2004, 2010 and 2014) were conducted on samples of the sliding surfaces to investigate the influencing factors on the landslide dam formation, particularly to present their shear characteristics. Furthermore, the test results were analyzed to clarify the mechanism of the rapid rainfall-induced
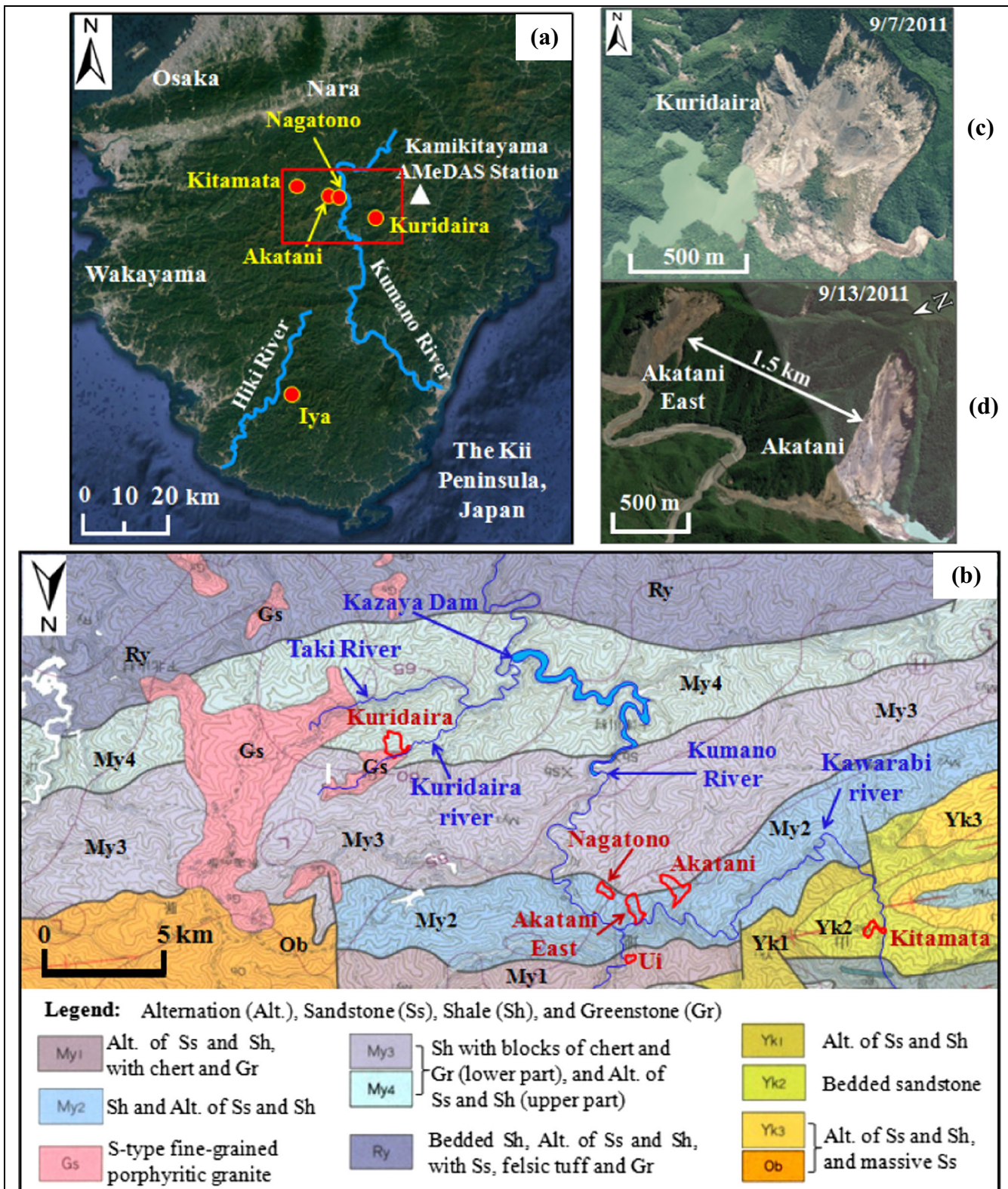
Fig. 1 **a** Location of five biggest landslide dams in the Kii Peninsula (indicated in yellow text). **b** Geological map (GSJ 1998) showing locations of two cases studies (Kuridaira and Akatani) and other landslide dams. **c** Aerial photograph of the Kuridaira landslide dam (by the Kii Mountain District Sabo Office). **d** Google Earth image of the Akatani landslide dam
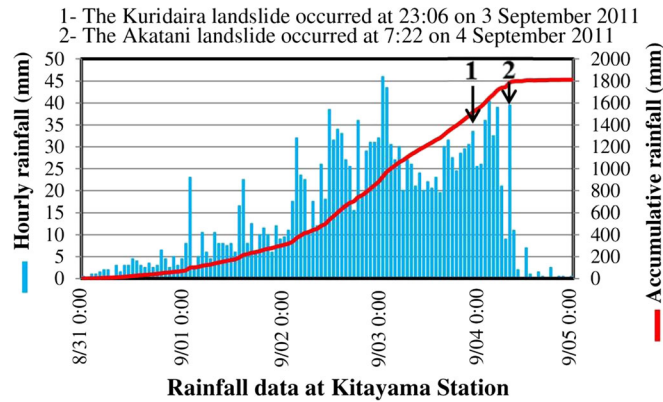
1- The Kuridaira landslide occurred at 23:06 on 3 September 2011
2- The Akatani landslide occurred at 7:22 on 4 September 2011

**Rainfall data at Kitayama Station**

**Fig. 2** Rainfall data at Kitayama AMeDAS Station from August 31 to September 4, 2011 (JMA 2011)

landslides. The initiation and motion processes leading to the landslide dam formation have not been observed and described to date. Computer simulation reproducing reliable formation process of the two landslide dams was thus performed by using an integrated simulation model with LS-RAPID software (Sassa et al. 2010).

From the points of view of the study, site surveys and soil sampling were first conducted to examine the geological and topographical characteristics and current situation of the landslides. Total unit weight of the collected soil samples was measured under a consolidation condition in ring shear apparatus. Subsequently, the deep-seated landslides, induced by pore water pressure increments due to rainfall or shear displacement along the sliding plane on gravitationally deformed slopes, were reproduced by using the mean of the high-stress dynamic-loading ring-shear

apparatus ICL-2. In this study, all of the tests were conducted on fully saturated samples with the saturation degree ($B_D$) equal to or larger than 0.95 because a high degree of saturation is necessary for acquiring the most accurate monitoring data. The $B_D$ value was calculated by using the values of excess pore pressure and normal stress increments under undrained conditions (Sassa et al. 2014). The maximum normal stress values of 1.5 and 1.0 MPa were given to the ring-shear tests, which corresponded to the sliding surface depth of more than 100 m for the Kuridaira and nearly 70 m for the Akatani landslide (SABO 2015). The samples were sheared in different shearing control modes, including undrained shear stress control (SSC), undrained shear displacement control (SDC), and drained pore water pressure control (PWP) tests. The latter tests indirectly simulated the buildup of the groundwater table under rainfall. The SSC tests were employed to measure soil parameters
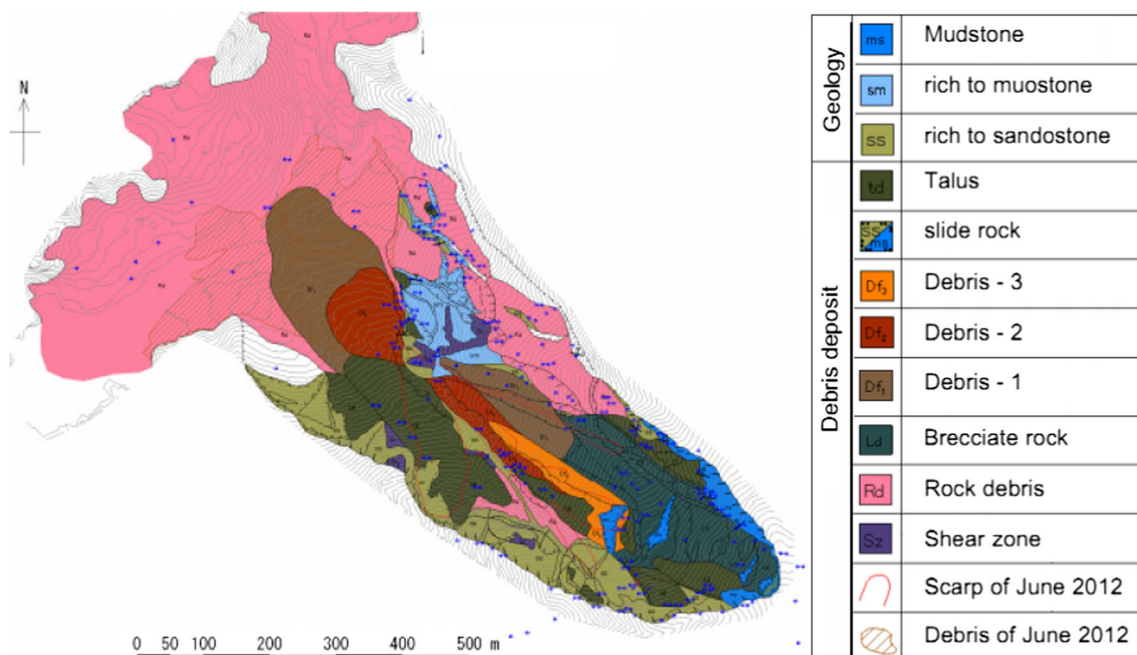


| Geology | | |
|---|---|---|
| ms | Mudstone | |
| sm | rich to muostone | |
| ss | rich to sandostone | |

| Debris deposit | | |
|---|---|---|
| td | Talus | |
| ss/m | slide rock | |
| Df₃ | Debris - 3 | |
| Df₂ | Debris - 2 | |
| Df₁ | Debris - 1 | |
| Ld | Brecciate rock | |
| Rd | Rock debris | |
| Sz | Shear zone | |
| ⌒ | Scarp of June 2012 | |
| ▨ | Debris of June 2012 | |

0  50  100    200    300    400    500 m

**Fig. 3** Morphological features of the Akatani landslide area (SABO 2014b)
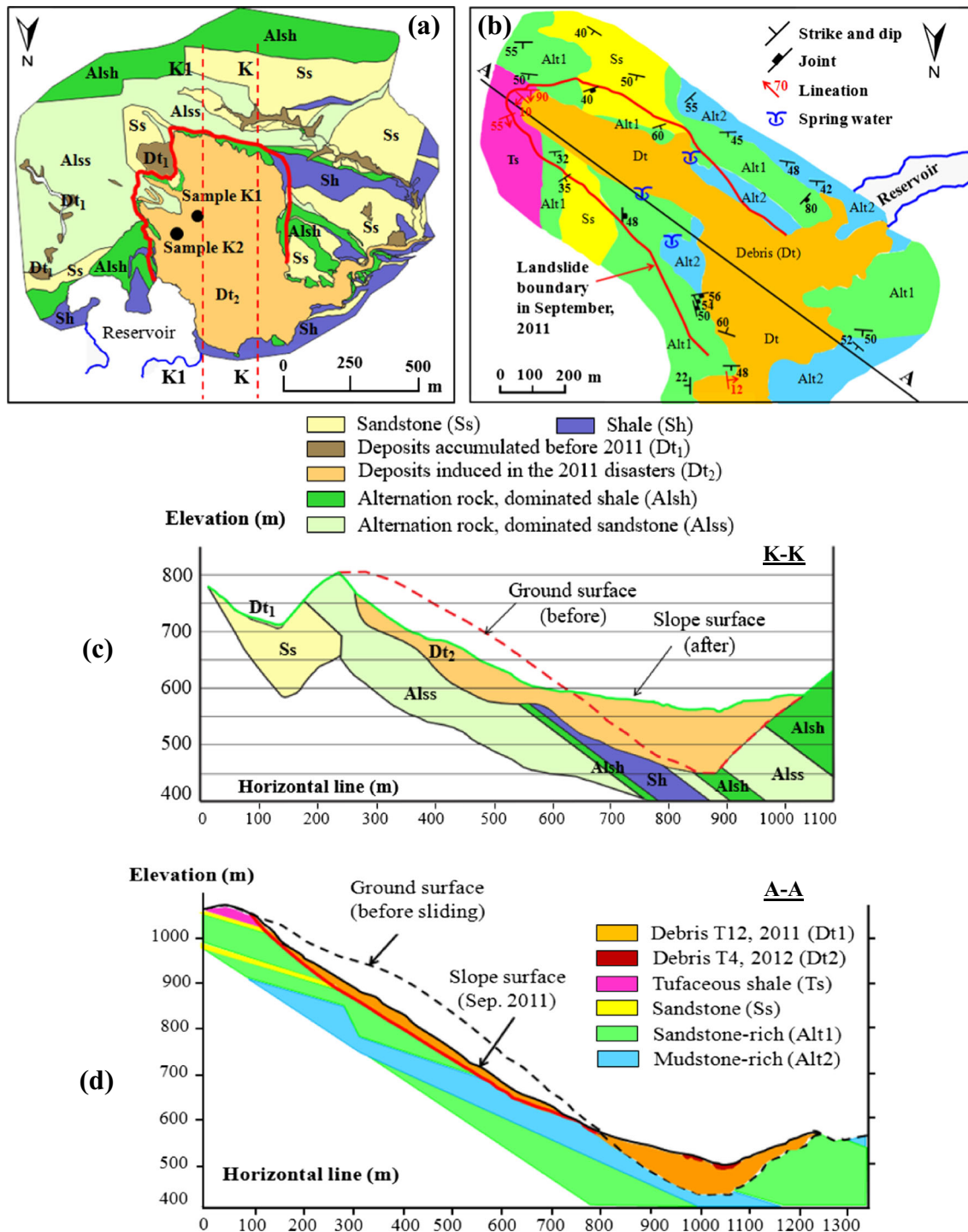
**Fig. 4** **a**, **b** Geological plans and **c**, **d** cross-section of two slopes after sliding for the Kuridaira landslide and Akatani landslide, respectively (modified from Kii Mountain District Sabo Office, SABO 2014a, 2014b)

and to monitor the reduction of shear stress and pore water pressure generation in a progress of accelerated shear displacement from pre-failure, through failure and transient state to steady state. The SDC tests were not only appropriate for investigating how a shear displacement would trigger a landslide, but they also measured physical parameters of the soil samples with low permeability accurately. Only the rainfall-induced landslide simulation by PWP tests is considered under the drained condition because waters can introduce into or come out of the shear box via the supply valve for pore water pressure. A detailed description and testing procedure of the apparatus ICL-2 are presented in Sassa et al. (2010, 2014).

Finally, a numerical simulation model of the two deep-seated catastrophic landslides was performed by using LS-RAPID software. The model integrates the initiation and motion processes of landslides triggered by rainfall and/or earthquake, respectively, from the stable state through the failure to post-failure at the steady state (Sassa et al. 2010, 2014). This model considers all driving forces acting on a moving landslide mass, i.e., self-weight, lateral pressure, shear resistance, seismic forces, and pore pressure. The initiation process and the development process to a rapid motion is the expression of strength reduction during deformation and the progressive failure. In the model, 10-m DEM data of the slope surfaces before landslides were from the Geospatial Information Authority of Japan (GSI 2011). The 10-m mesh data of the sliding surface after the landslide event was based on 5-m DEM data created by SABO in 2011. The model employs a triggering factor of pore water pressure indirectly simulating the increment of groundwater level under rainfall. Most of the soil parameters measured from ring-shear experiments were used as an input for the computer simulation, whereas other parameters were assumed according to the site investigation or likely conditions of the landslides. In the model, input parameters of the samples were set according to the geological distribution along the sliding surfaces based on the profiles of slopes after sliding (Fig. 3) and site investigation (Figs. 4 and 5). For the Kuridaira landslide area, shear parameters of sample K2 were applied to the right flank and in the lower part near the toe of the slope, while other areas used physical properties of sample K1. In the case of the Akatani landslide area, parameters of sample A1 were given to the entire area of the sliding surface except to the areas of right head scarp and the lower part near the toe where sample A2 was located.

### Site investigation and soil properties

Geological and morphological features of the landslide areas were examined during the site survey. On-site evidence indicates that the large deep-seated landslides with undulatory sliding surfaces occurred as rockslide-avalanches on thickly vegetated, steep slopes in the narrow V-shaped valleys. The sliding surfaces formed along the dip direction of the strata on the planes of weakness, such as faults or bedding planes. Large mass movements then have completely obstructed the river channels to form lake basins upstream. The formation of the two landslide dams and their impoundments were created in the tributaries of the Kumano River (Fig. 1). Failure characteristics of the landslide dams are presented in Figs. 5 and 6.

Figure 5a, taken in May 2015, presents an overview of the deep-seated Kuridaira landslide. The geological structure of the slope is characterized by clastic debris materials produced from fractured shale and sandstone-dominated rock masses or their interbedded layers. Shale and shale-dominated rock bodies are distributed at the right flank and near the V-shaped head scarp, while the distribution of sandstone-dominated rocks largely extends from the left flank to the middle part of the slope. The sliding surface, consisting of interbedded sandstone and shale layers, is found near the head scarp (Fig. 5c). The liquefied materials within the shear zone (Fig. 5d) imply that the rapid movement of the landslide triggered by excess pore water pressure due to grain crushing of sliding plane materials. Two soil samples of the sliding surface in sandstone and shale layers

were taken to investigate the failure mechanism of the landslide. The locations and photographs of the soil sampling are shown in Fig. 5a, b. These are sandstone-dominated material samples such as clayed sand (sample K1) and fractured shale samples (sample K2). Sample K1 has low permeability and is finer than sample K2. Sample K1 contains coarse-grained clastic rocks and a small proportion of brown clay-sized materials. Conversely, sample K2 contains small grain-sized, angular, black-greenish fragments of broken shale; the color of sample K2 later changed to yellow to some extent. Moreover, sample K2 is brittle, fissile, and easy to break by hand. In the ring-shear tests, sample K2 is highly deformed under high normal stress during consolidation. A grain-size distribution of samples K1 and K2 is presented in Fig. 7.

Figure 6 shows landslides in the Akatani valley where two natural dams were created by massive movements. The Akatani East landslide dam, which is 1.5 km downstream of the Akatani landslide dam (Fig. 1d), was breached just after a river blocking. The surface of this landslide is a brown color, because soil materials are fully deoxidized when saturated by surface water flow. Materials of the sliding surface and debris masses are easy to observe in the landslide areas. For the Akatani landslide, sandstone-rich materials are largely distributed on the sliding plane, while mudstone-rich materials are only found in the top right part of the head scarp and in the area near the toe (Fig. 6a). The Akatani landslide has continuously been at risk from overtopping, dam erosions, and the downward movement of unstable debris masses reposing on the sliding plane. There are therefore limitations, mostly for safety reasons, to collecting soil samples or closely observing the failure characteristics within the Akatani landslide area. Consequently, it was decided to conduct an in-depth site survey and soil sampling in the Akatani East landslide because of its similarity in geology and morphology to the slopes in the Akatani valley (Tien et al. 2017). In the survey, notable evidence of water springs (Fig. 6a, b) on the sliding surfaces implies the contribution of a high groundwater table, resulting from high rainfall, as the main trigger of the landslides.

The Akatani East landslide's sliding surface is formed along the dip direction of the strata of interbedded sandstone- and mudstone-rich material layers (Figs. 4b, d and 6b). Therefore, soil samples of the sliding surface that had similar geological features to those of the Akatani landslide were collected at the sliding surface of the Akatani East landslide area. As shown in Fig. 6b, two locations are examined for soil sampling: A1, locates within a fault gouge in the interbedded sandstone- and mudstone-rich blocks (Fig. 6c), and A2, which contains landslide debris of dark-gray mudstone-rich materials (Fig. 6d). At location A1, two separately observed layers are the upper layer of dark-gray mudstone-rich materials and the lower layer of light-gray sandstone-rich materials. Both materials are produced via grain crushing of interbedded layers of sandstone and mudstone due to tectonic activities along the fault. The upper layer is thinner and its grain size is finer than that of the lower layer. The upper layer material is very similar to the residual debris at location A2 (Tien et al. 2017). Therefore, only two soil specimens are used in ring-shear tests, namely the sandstone-rich sample (sample A1) and the mudstone-rich sample (sample A2). The grain-size distribution of these samples (Fig. 7) indicates that both samples contain clay- and silt-sized grains, where sample A2 is finer than A1.
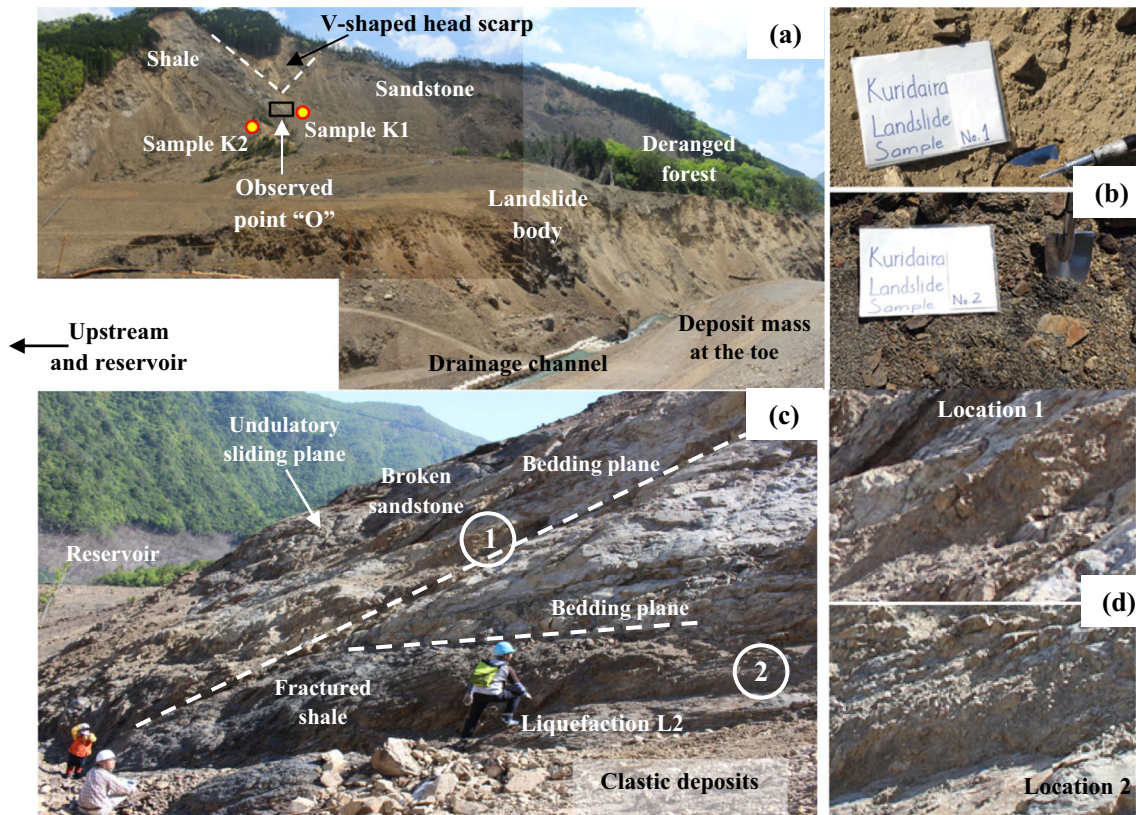
**Fig. 5 a** Overview of the Kuridaira landslide. **b** Photographs of soil sampling. **c** Observed point "O" shows undulatory sliding surface with interbedded shale and sandstone layers. **d** Evidence of grain crushing

### Ring-shear tests and results

#### The Kuridaira landslide

Undrained SSC and SDC tests
Both SSC and SDC tests are conducted on samples K1 and K2 under three different normal stresses ($\sigma$) of 0.5, 1, and 1.5 MPa. For each test, the sample is first consolidated at the designed normal stress in the drained condition. Shear stress is then applied gradually at a given rate ($\Delta \tau / s$) of 1–2 kPa/s until the failure in the SSC tests, or the sample is immediately sheared at a designed shearing

velocity ($S_v$) of 0.1 mm/s in SDC tests. The time series data and stress paths for samples K1 and K2 are indicated in Figs. 8 and 9, respectively.

The test results indicate that the landslides occur as the effective stress path reaches the failure line (Figs. 8-right and 9-right). In SDC tests, samples fail to initiate the landslide motion at a small shear displacement. After sliding, the shear strength quickly reduces in the accelerating progress of shear displacement due to excess pore water pressure generation resulting from extensive grain crushing (Fukuoka et al. 2006 and 2007). Rapid motion is observed when sliding surface liquefaction (Sassa 1996) takes
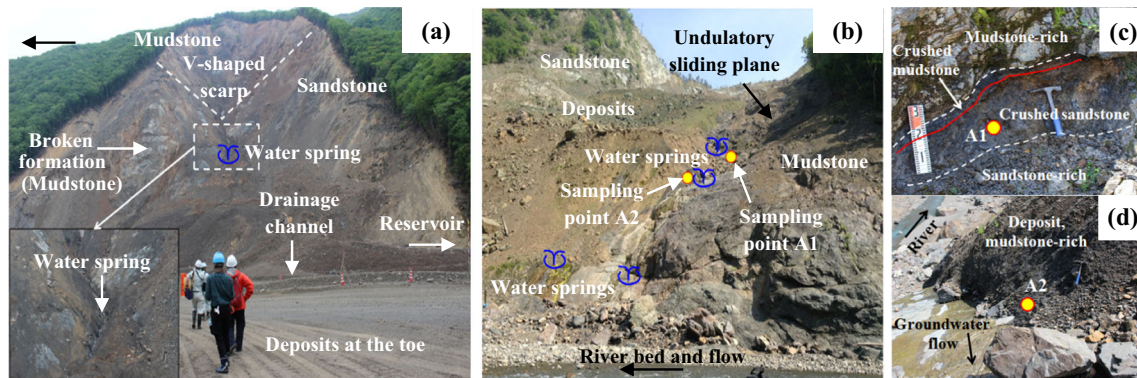


**Fig. 6** Photographs of site survey for **a** the Akatani landslide and **b** the Akatani East landslide, and photographs of soil sampling at **c** point A1 and **d** point A2
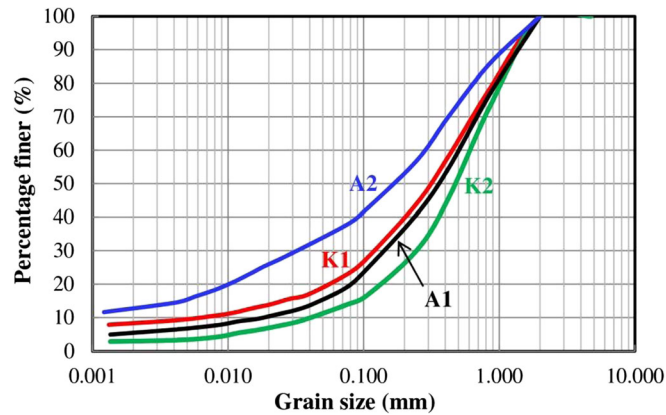
**Fig. 7** Grain-size distribution of tested soil samples from the Akatani-East landslide (A1 and A2) and the Kuridaira landslide (K1 and K2)

place, in particular to sample K2 tests. The shear stress continues moving along the failure line to certain values of the steady-state shear resistance. The mean values of the friction angle both during motion and at peak are 38.5 and 41.2° for sample K1 (Fig. 10a) and 41.5 and 44.1° for sample K2 (Fig. 10b).

The test results imply that sample K2 exhibits behavior of granular materials: incessant grain crushing, rapid excess pore pressure generation, and a high drop of shear strength. As a result, residual strengths of sample K2 are low at 25, 37, and 95 kPa, and the highest mobilized apparent friction angle is only 3.7° (Fig. 10b). Sample K1 is close to sliding surface liquefaction at 0.5 MPa (Fig. 8a). Since there is no much shear strength reduction for sample K1 under 1.0 and 1.5 MPa tests, partial sliding surface liquefaction is observed due to a potential susceptibility of its coarse grain-size to grain crushing. A small decrease in pore water pressure is monitored in sample K1 tests after the shear stress reaches certain values at the steady state (Fig. 8b, c). The mobilized shear resistances of sample K1 are 53, 235, and 412 kPa in 0.5, 1.0, and 1.5 MPa tests, respectively. The mobilized apparent friction angle of this sample is 6.5–15.6° (Figs. 8a and 10a). Combined effective stress paths for samples K1 and K2 tests are depicted in Fig. 9.

PWP tests simulating rainfall-induced landslide
In this simulation, the saturated samples are first consolidated to 1.0 MPa normal stress and 0.6 MPa shear stress in the drained condition. The initial stresses (black line in Fig. 11) are estimated from a representative sliding plane depth of about 70 m at the Kuridaira slope with an inclination of 31° and soil weight of approximately 20 kN/m$^3$. The rainfall-induced landslide is indirectly simulated by the gradual increment of pore water pressure at a rate of 1 kPa/s. The results displayed in Fig. 11 present landslides occurring at pore water pressure values of 330 and 360 kPa for samples K1 and K2, respectively. This means that the pore water pressure ratios due to rainfall are 0.33–0.36. Rapidly moving landslides are subsequently observed due to excess pore water pressure generation coupled with a sudden drop in shear resistance in the progress of shear

displacement. In these drained tests, a high generated excess pore water pressure is not measured due to its dissipation through the supply valve for pore water pressure. Some excess pore water pressure is partly monitored because the generation rate is larger than the dissipation rate.

**The Akatani landslide**

Undrained SDC tests
In the simulations, the Akatani samples are consolidated at normal stresses of 0.8 MPa and are subsequently instantly sheared at a low shear displacement rate of 0.1 mm/s for sample A1 and 0.05 mm/s for sample A2. Figure 12 shows that excess pore water pressure generation is immediately monitored under a small shear displacement (shear displacement at failure) in the undrained SDC tests. Sample A1 produces much excess pore pressure and obtained friction angles of 39.5° during motion. The residual strength at the steady state is 150 kPa (Fig. 12a), while the apparent friction angle is about 13.0°. For sample A2, excess pore water pressure is generated due to shear deformation just after shearing loading and temporarily maintained with no grain crushing. Although water leakage does not appear, pore water pressure then starts to decrease to almost zero at a large shear displacement. The end point of mobilized shear resistance is close to the initial shear stresses (Fig. 12b). The friction angle during motion is about 38.0° and is reduced to 30.0° as the apparent friction angle at the steady state. The shearing stops at a shear displacement of 2500 mm for both tests.

PWP tests simulating rainfall-induced landslide
In the PWP tests, the initial stress conditions are reproduced at 1000 kPa of normal stress and 620 kPa of shear stress. The pore water pressure increment simulating the rainfall-induced landslide is maintained at a constant rate of 0.5 kPa/s for sample A1 and 1 kPa/s for sample A2 (Fig. 13). The ratio of shear stress to normal stress is about 0.62, corresponding to the natural slope angle of 34°. The failure of samples A1 and A2 is initiated when
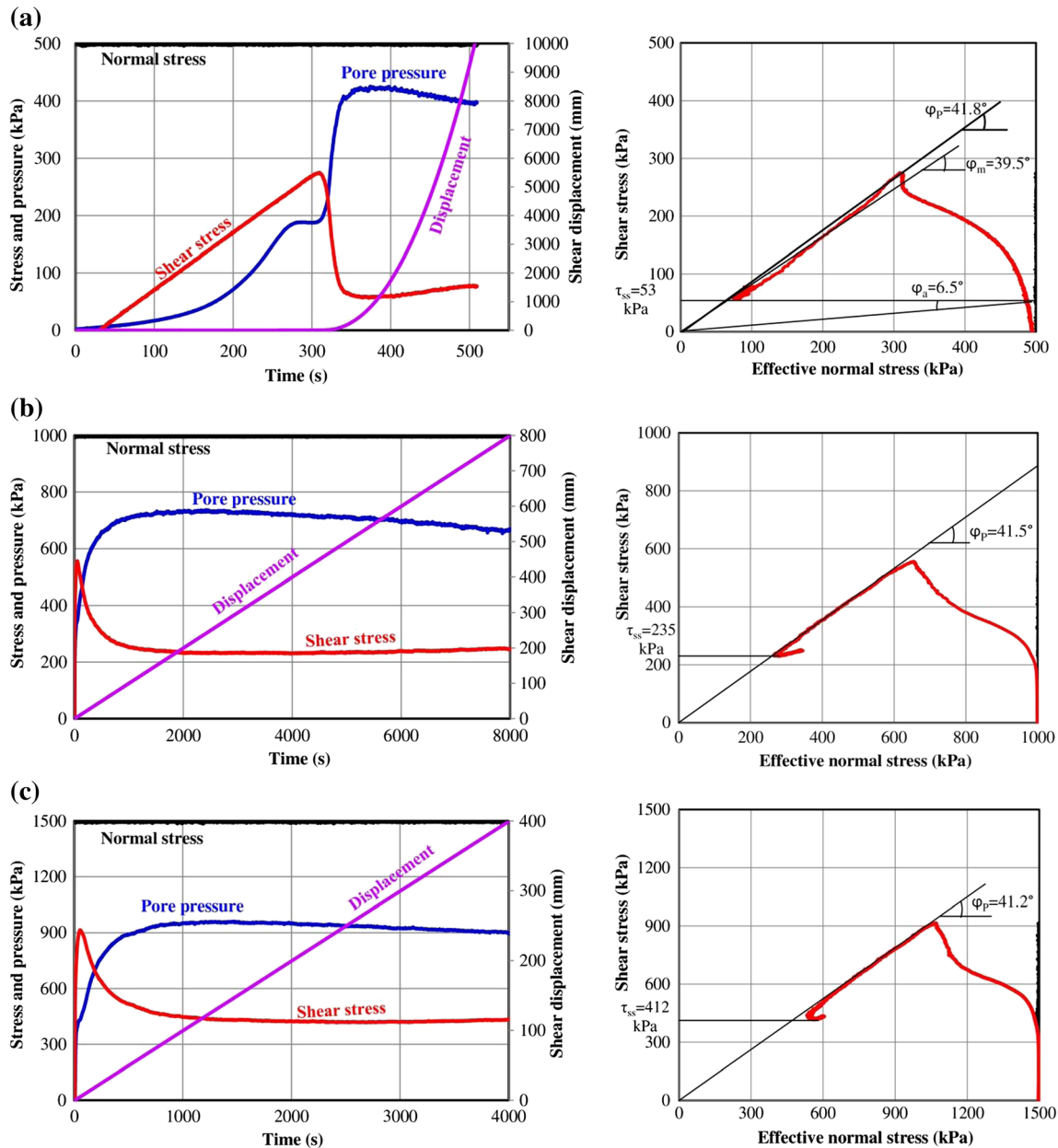
**Fig. 8** Time series data (left) and stress paths (right) of ring-shear tests on sample K1 from the Kuridaira landslide at different normal stresses: **a** shear stress control test at σ = 0.5 MPa, $B_D$ = 0.96, Δτ/s = 1 kPa/s; **b** shear displacement control test at σ = 1.0 MPa, $B_D$ = 0.96, Sv = 0.01 cm/s; **c** shear displacement control test at σ = 1.5 MPa, $B_D$ = 0.96, Sv = 0.01 cm/s

controlled pore pressure values reach 340 and 370 kPa, respectively. This means that the critical pore water pressure ratio ($r_u$) that triggered the landslide is 0.34–0.37. Sample A1 has a high level of landslide mobility because of the great loss of shear resistance under a rainfall simulation (Fig. 13a), whereas sample A2 shows a lack of mobility (Fig. 13b). After failure, sample A1 stays at a small apparent friction angle of 5.5°, whereas this value is 14.8° for sample A2. Accordingly, the rapid motion of the Akatani landslide is mainly attributed to a large shear reduction of sample A1, while sample A2 does not play a critical role.

**Shear strength reduction in the progress of shear displacement**

The relation of shear strength reduction in the progress of shear displacement is presented in Fig. 14. The $D_L$ value defines the shear displacement at the starting point of shear strength reduction (at peak strength), and the $D_U$ value indicates the shear displacement at the end point of shear strength reduction (the shear strength for the initiation of steady-state shear resistance). The sample failure experiences four main periods, namely pre-failure, failure, transient, and steady states (Sassa et al. 2010), that are separated by the $D_L$ and $D_U$ values. The analysis shows $D_L$ and $D_U$ values of 2–6 and
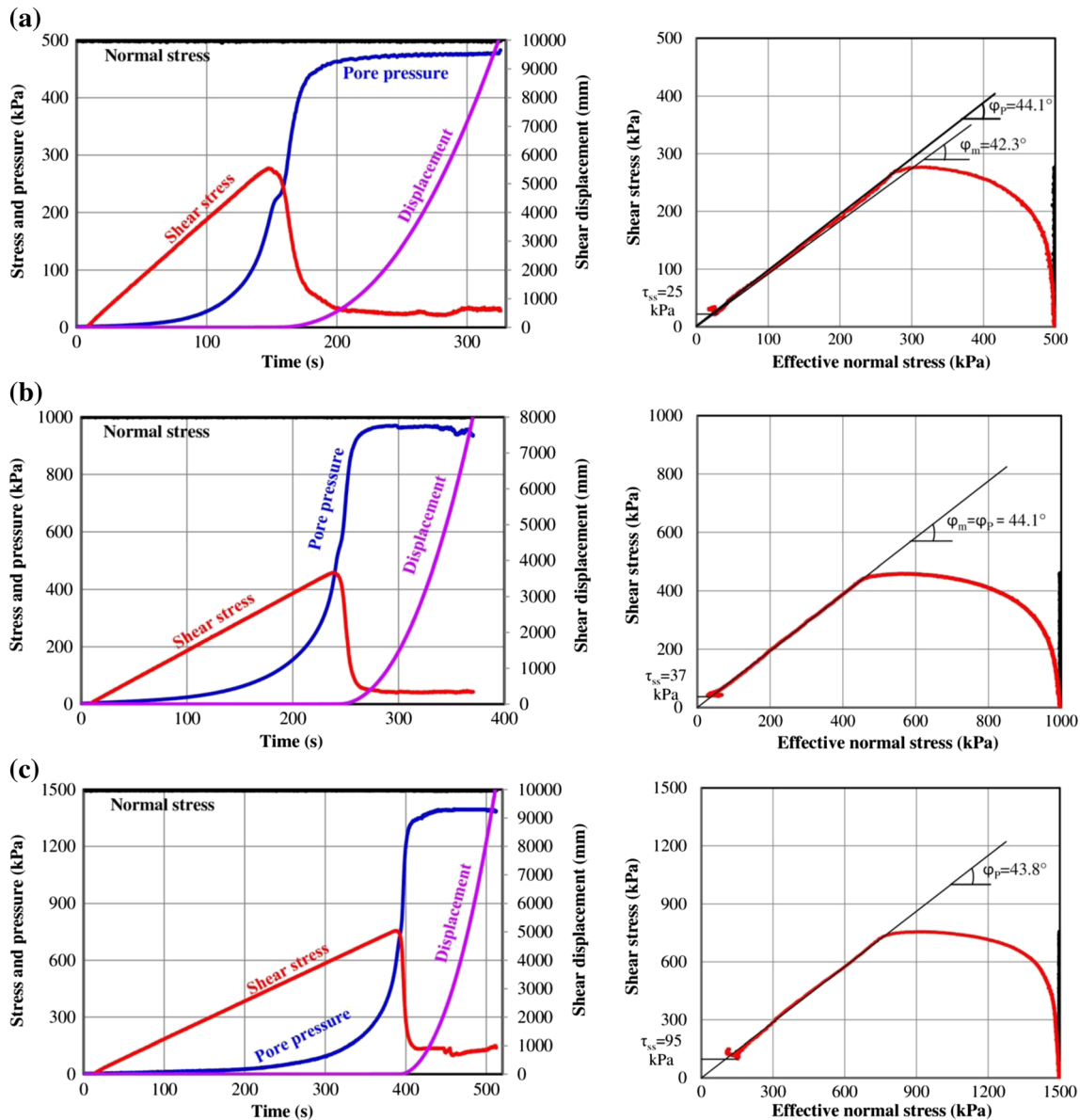
**Fig. 9** Time series data (left) and stress path (right) of SSC tests on sample K2 from the Kuridaira landslide at different normal stresses (σ) with shear stress increment $\Delta\tau/s = 2$ kPa/s: **a** σ = 0.5 MPa, $B_D$ = 0.96. **b** σ = 1.0 MPa, $B_D$ = 0.96. c) σ = 1.5 MPa, $B_D$ = 0.96

80–200 mm, respectively, for Kuridaira samples and $D_L$ and $D_U$ values of 4–7 and 500–1500 mm for Akatani samples.

**Integrated computer simulation model for the two massive landslides**
To simulate the two massive landslides induced by rainfall, the LS-RAPID model is conducted by using soil parameters (Table 1) obtained from the ring-shear tests. The following are detailed explanations of indispensable input parameters:

- Lateral pressure ratio (k): The ratio is estimated to be 0.3–0.35 for the Kuridaira landslide and 0.35–0.42 for the Akatani landslide. The smaller value is for the lower part and the toe.
- $D_U$ and $D_L$ values: These parameters use the average values presented in Fig. 14.

- Steady-state shear resistance ($\tau_{ss}$): This parameter varies and depends on soil depth at sliding surfaces. The values of 53–412 and 25–95 kPa are used for sandstone and shale rock areas of Kuridaira slope (Figs. 8 and 9). Values ranging from 94.5 to 150 kPa and from 265 to 400 kPa are employed for sandstone and mudstone areas of the Akatani slope (Figs. 12 and 13). A higher value corresponds to a higher depth of the sliding surfaces.
- Excess pore water pressure generation ($B_{ss}$): The $B_{ss}$ value of each area on the slope depends on the degree of saturation resulting from the groundwater level. This parameter is selected to range from 0.25 to 0.80 for the Kuridaira landslide and from 0.25 to 0.85 for the Akatani landslide. In the model, we use a $B_{ss}$ of 0.25–0.45 for parts of the head scarp due to lower
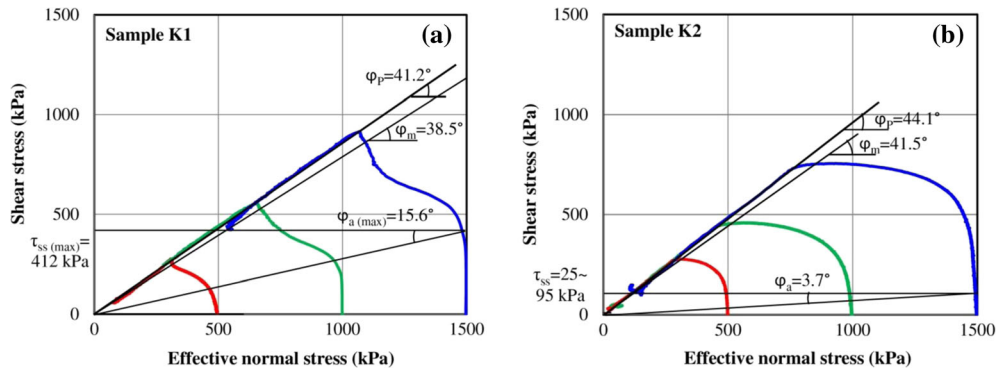
**Fig. 10** Combined effective stress paths: **a** sample K1 and **b** sample K2 from the Kuridaira landslide

saturation and a higher value of 0.5–0.75 for the middle part, while a very high value of 0.75–0.85 is used for the toe and lower part of the slope.

- Peak cohesion before motion ($C_p$): Since two catastrophic deep-seated landslides occur along bedding rocks of sandstone, shale, and mudstones, we employ the value of $C_p$ ranging from 250 to 300 kPa.
- Pore-water pressure ratio ($r_u$): According to the test results, the Kuridaira and Akatani landslides are triggered by rainfall with critical pore water pressure ratios ranging from 0.33 to 0.36 and 0.33 to 0.37, respectively. We first conduct testing models with variable values of $r_u$ for both landslides. After

doing a validation and calibration, pore water pressure ratios, due to rainfall triggering the Kuridaira and Akatani landslides, are found to be 0.33 and 0.36, respectively. In the simulation, the time increment is set to 10 s and the loading duration is 150 s.

The entire formation process of the two massive landslide dams during heavy rainfall is summarized in Table 2. These processes experience four main stages (Fig. 14): from the stable state to local failure and through the transient state (progressive failures) before reaching the post-failure stage (acceleration of rapid motion and stopping of motion) at the steady state. The blue zones in Table 2
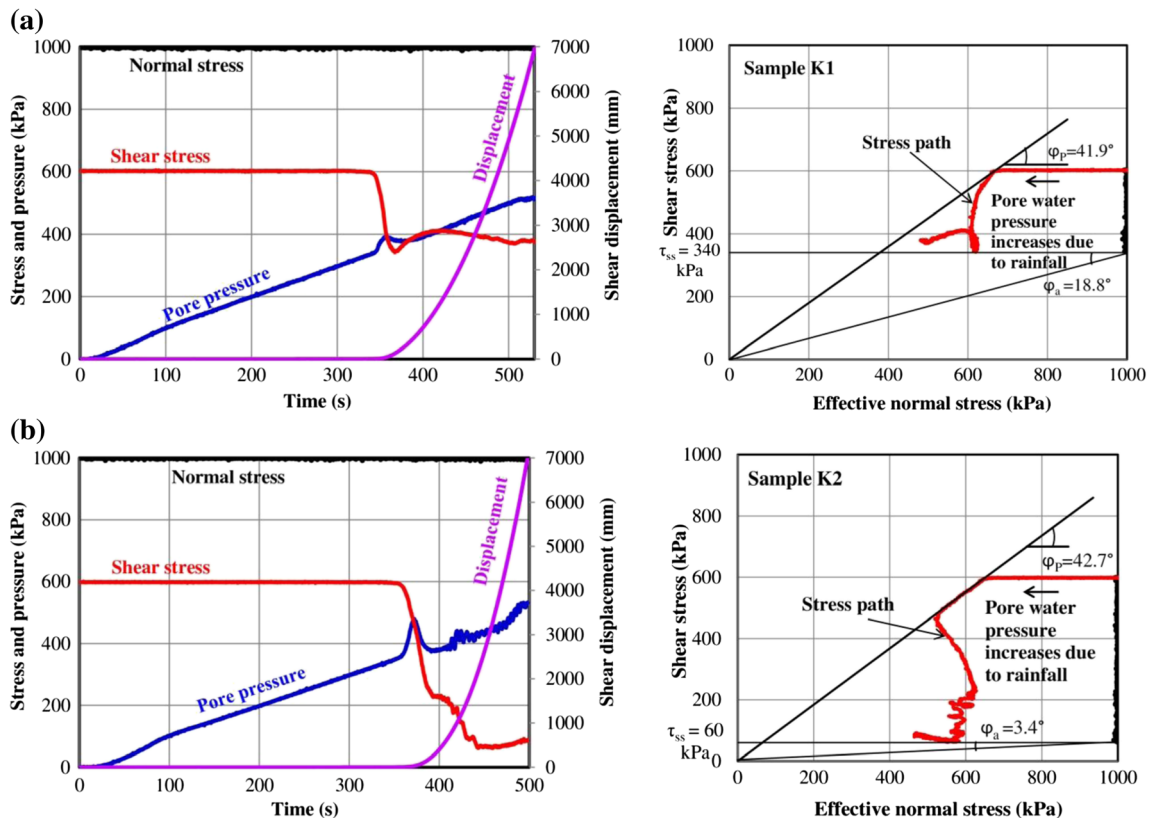


**Fig. 11** PWP tests for rainfall-induced landslide: **a** sample K1 and **b** sample K2 from the Kuridaira landslide
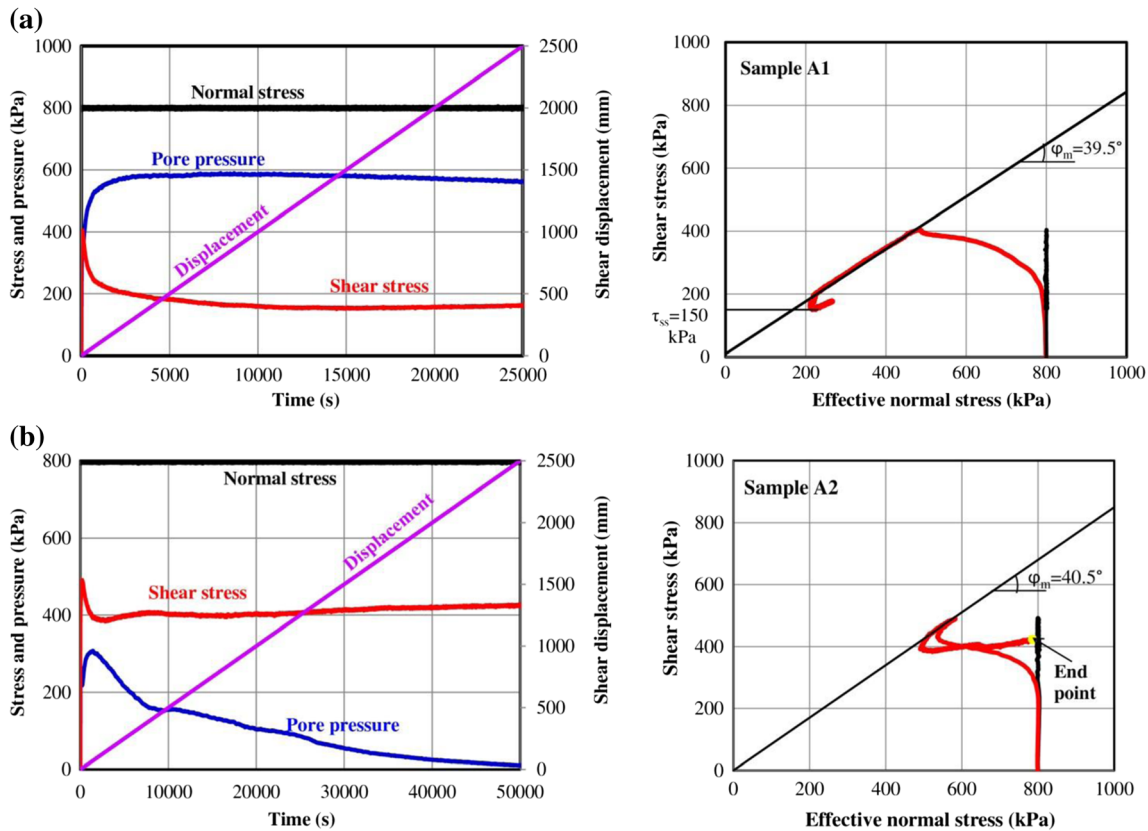
Fig. 12 Results of the SDC tests with time series data (left) and effective stress path (right): **a** sample A1 and **b** sample A2 from the Akatani landslide

represent stable parts, whereas the red zones display unstable parts as any failure occurs. The landslide dam formation and its motion behaviors are described below:

At the pre-failure state, slopes remain stable before the pore water pressure reaches the critical value at the 10th second (Table 2a). When the pore pressure ratio within the slopes rises to critical values during a heavy rainfall event, the initial local failures (red points in the mesh) are initiated from the area of samples K2 and A1 in the lower middle parts of the Kuridaira and Akatani landslide bodies, respectively (Table 2b). The location of the initiation of the landslides is in the same area in a large number of testing models. In the simulation, the pore pressure ratio values are kept constant at $r_u = 0.33$ for the Kuridaira and $r_u = 0.36$ for the Akatani landslides from 11th second to the end of sliding. The failure expands to the adjacent points and gradually spread to a large area of landslide bodies. The slopes then start to move down at 19.1 and 19.5 s for the Kuridaira and Akatani landslides, respectively (Table 2c). The progressive failures resulting from local failure points are caused by a downward movement of their upper zones, due to losing support at the bases, and lower zones, due to the dynamic effects of the upper parts. This process quickly continues and exacerbates the failure in the entire slope. At the steady state, rapid motions accelerate due to a great loss of shear strength and excess pore water pressure. The large-scale landslides travel at high speeds down the valleys (Table 2d). Subsequently, the landslide debris is channeled along moving paths and rushed down to the toe. The large volume of landslide masses completely dams the river courses and forms

reservoirs in Kuridaira and Akatani valleys. In the last duration, the motions gradually decelerate and stop after 104 and 110.3 s in the respective valleys (Table 2e).

The maximum velocity of mass movements by simulation time and along the sections K-K, K1-K1, and A-A (Fig. 4) are performed for the Kuridaira and Akatani landslides in Fig. 15. The maximum speeds of the Kuridaira and Akatani landslide motions are 42.8 and 51.8 m/s at 45 and 36 s, respectively, before the landslide bodies collide with the opposite wall (Table 2d). The model closely matches corresponding Google Earth images. The simulated results from the model nearly exactly overlap the images of the landslide source area and the accumulation zone in the river valleys (Table 2e). In addition, cross-sections obtained from the model and the DEM data provided by the SABO Office after the landslide in 2011 (SABO 2015, Fig. 16) are compared.

### Discussion

Slow-moving landslides have mostly been characterized in sedimentary zones composed of mudstones and green schist, such as the Shikoku Region, West Japan (Bhandary and Yatabe 2007), or formed in weak mudstone of the Neogene sedimentary strata in the Kii Peninsula, Japan (Chigira 2015; Chigira et al. 2016). This typical feature is attributed to the influence of clay-sized minerals of the sliding surface materials that are not susceptible to grain crushing. Sliding surface liquefaction (Sassa 1996) would not take place because of the lack of excess pore water pressure generation due to no grain crushing (Fukuoka et al. 2006). Consequently, landslides would not show a high mobility level for traveling at
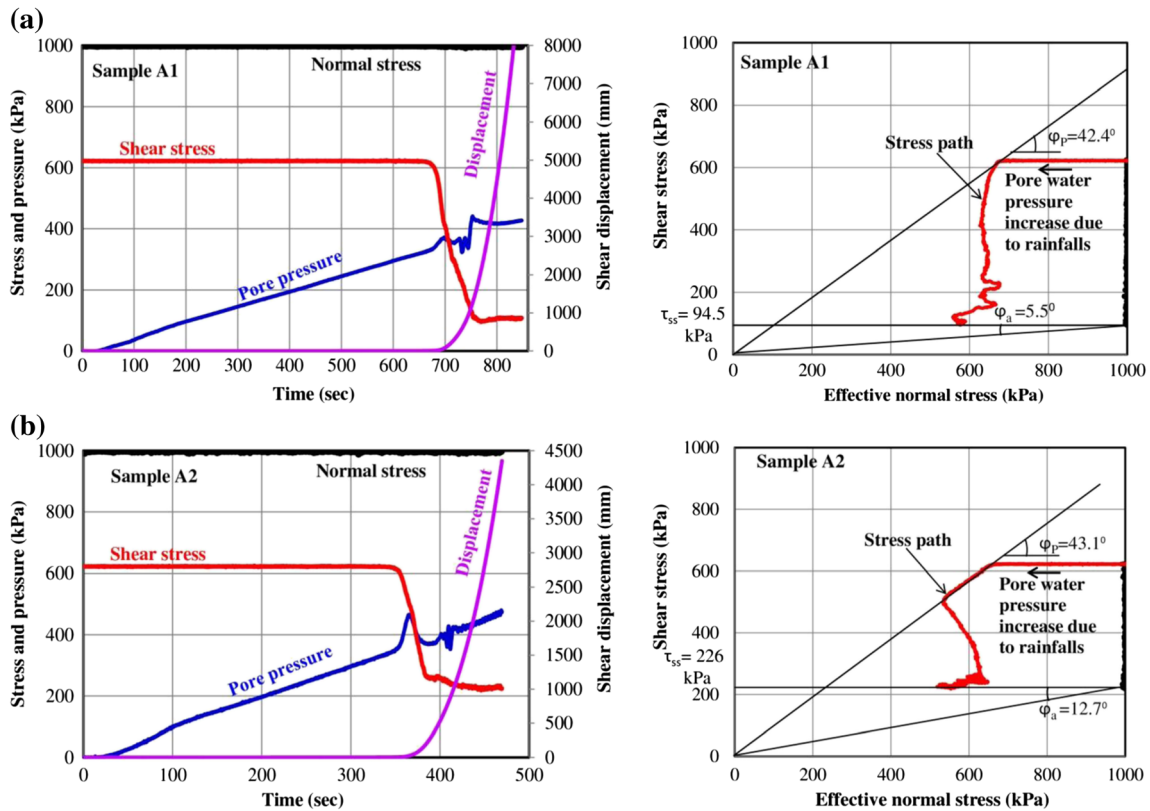
**Fig. 13** PWP tests for rainfall-induced landslide: **a** sample A1 and **b** sample A2 from the Akatani landslide

high velocities in the geological setting of mudstone and/or shale. The finding on the mechanism of rapid landslides in the Kuridaira and Akatani slopes is presented in this study. Ring-shear tests point out that the rapid moving landslides are mainly governed by mobility behavior due to sliding surface liquefaction of fractured shale rocks (sample K2) and sandstone-rich material (sample A1) under pore water pressure and shear loading. The high-mobility behavior provokes the landslides to rapidly travel in a long run-out. The simulation highlights the contribution of high pore water pressure resulting from rainfall that triggered the landslides. Under pore water pressure loading, the shear strength reduces from a peak of 42.7° to an undrained-state residual friction

angle of 3.4° at the steady state for sample K2 and from 42.1 to 5.5° for sample A1. The sliding surface liquefaction (Fig. 17), caused by extensive grain crushing and excess pore water pressure generation, leads to the significant drop in the strengths of K2 and A1 samples. The shear behavior indicates high mobility of samples K2 and A1 during motion. Conversely, mudstone-rich material (sample A2) does not produce rapid motion because its fine-grained minerals are not subjected to grain crushing. In undrained SDC test, a temporary excess of pore water pressure appears and this amount of pore water pressure dissipates completely (Fig. 12b). The typical shear behavior is interpreted as follows: sample A2 contains a large proportion of expansive materials of clay-sized
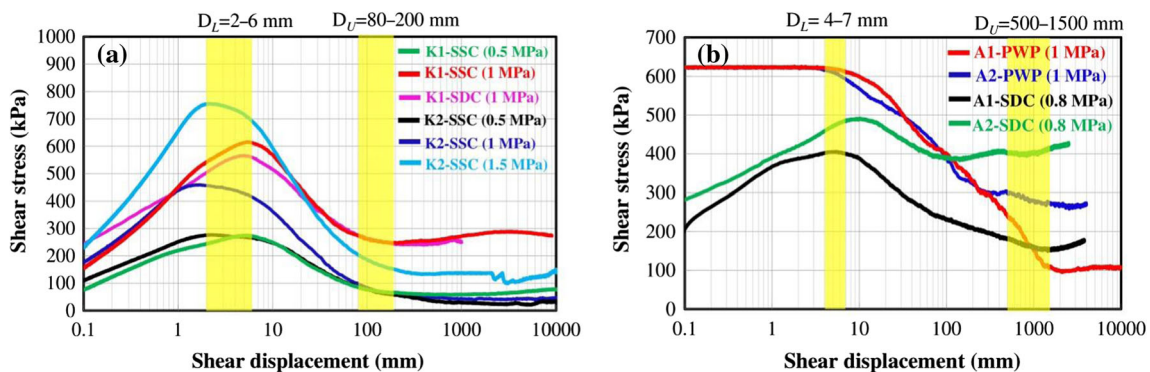


**Fig. 14** Shear strength reduction in the progress of shear displacement at normal stress of 1000 kPa: **a** Kuridaira samples (K1 and K2) and **b** Akatani samples (A1 and A2)

**Table 1** Soil parameters for computer simulation models

| Soil parameters | Value for the landslides | | | | Source |
|---|---|---|---|---|---|
| | Kuridaira (sandstone areas) | Kuridaira (shale areas) | Akatani (sandstone areas) | Akatani (mudstone areas) | |
| Material properties and shear strength parameters | | | | | |
| Total unit weight of the mass ($\gamma_t$, kN/m$^3$) | 20.0 | 19.5 | 20.2 | 20.6 | Test data |
| Unit weight of water ($\gamma_w$, kN/m$^3$) | 9.81 | 9.81 | 9.81 | 9.81 | Assumed |
| Lateral pressure ratio ($k = \sigma_h/\sigma_v$) | 0.3–0.35 | 0.35–0.35 | 0.35–0.42 | 0.35–0.42 | Estimated |
| Friction angle during motion ($\Phi_m$, °) | 38.5 | 41.5 | 39.5 | 40.5 | Test data |
| Peak friction angle ($\Phi_p$, °) | 41.2 | 44.1 | 42.1 | 43.2 | Test data |
| Steady state shear resistance ($\tau_{ss}$, kPa) | 53–412 | 25–95 | 94.5–150 | 265–400 | Test data |
| Peak cohesion at sliding surface ($c_p$, kPa) | 250–300 | 250–300 | 250–300 | 250–300 | Reference data |
| Shear displacement at the start of strength reduction ($D_L$, mm) | 4 | 4 | 6 | 6 | Test data |
| Shear displacement at the end of strength reduction ($D_U$, mm) | 140 | 140 | 1000 | 1000 | Test data |
| Pore pressure ratio ($r_u$) | 0.33 | 0.33 | 0.36 | 0.36 | Test data |
| Pore pressure generation rate ($B_{ss}$) | 0.25–0.85 | 0.25–0.85 | 0.25–0.9 | 0.25–0.9 | Estimated |
| Cohesion inside mass ($c_i$, kPa) | 0.1 | 0.1 | 0.1 | 0.1 | Assumed |
| Cohesion at sliding surface during motion ($c_m$, kPa) | 0.1 | 0.1 | 0.1 | 0.1 | Assumed |
| Parameters of the function for non-frictional energy consumption | | | | | |
| Coefficient for non-frictional energy consumption | 5 | 5 | 5 | 5 | Sassa et al. (2010) |
| Threshold value of velocity (m/s) | 80 | 80 | 80 | 80 | Record data |
| Threshold value of soil height (m) | 150 | 150 | 100 | 100 | Record data |

grains that are not highly susceptible to grain crushing under shearing. As a result, sample A2 does not crush to induce excess pore water pressure. The monitored pore water pressure is produced due to sudden shear displacement and incessant deformation of the sample within the shear zone. Consequently, this temporary pressure tends to be dissipated in a long time of the test. Under this condition, clay, silt, and fine-grained materials such as mudstone or mudstone-rich materials are not susceptible to high landslide mobility. Moreover, the experiments show that a certain amount of shear displacement of 2–7 mm accumulating along the sliding surface due to the impact of gravitational slope deformation could be an important factor triggering the landslides. As the shear displacement reaches a critical value ($D_L$ value), local soil deformation due to undrained compression is formed to induce excess pore water pressure, which is mainly responsible for the landslide. The gravitational slope deformation accelerates the rainwater infiltration, resulting in increased pore water pressure above the bedrock and triggering the failures. Together with this typical effect, the experiment results strongly demonstrate that slope deformation might act on the potential sliding surface to create small shear displacements and deformations as a trigger of the landslides.

In the computer model, the two slopes initiate failing at the lower middle area of the slopes. Compared to the geological distribution of the landslides, the landslide onset corresponds to the areas of the high-mobility samples K2 and A1 and is located in the areas with a sudden change in the geological boundary (Fig. 4). Simulation results reveal that the high potential of the landslide initiation is in the high-mobility layers of the sliding surface. In the specific cases of the two studied landslides, the sliding is initiated at the boundary areas between interbedded sandstone and shale materials for the Kuridaira landslide and interbedded sandstone and mudstone materials for the Akatani landslide. The shear strength of materials of the interbedded layers is possibly weak in the boundary areas due to the absence of interlocking and bonding materials. Similar results are obtained from a large number of simulations of the two landslides with the LS-RAPID model, which indicate that the abovementioned interpretations are appropriate for the initiation position. In comparison to the Kuridaira landslide velocity, the Akatani landslide moves at a higher speed because of its steeper topography. Although samples K2 and A1 show high-mobility effects due to their small mobilized apparent frictions, the mass movements stop at the toes of the slopes instead of traveling further than expected. This is due to the

**Table 2** Description of the entire formation process of the Kuridaira and Akatani landslide dams

| Stage/description | Images of the landslide dam formation process | | |
|---|---|---|---|
| | Kuridaira landslide dam | Akatani landslide dam | |
| **Pre-failure** Slopes were still stable if pore water pressure ratios ($r_u$) due to rainfall were smaller than critical values | $r_u$<0.33 | $r_u$<0.36 | **(a)** |
| **Failure** Initial local failures occurred on the slopes when $r_u$ constantly reached the critical values. Small movements were initiated to move downward | $r_u$=0.33 | $r_u$=0.36 | **(b)** |
| **Transient state with progressive failures** Local failures were expanded to adjacent areas. Progressive failures occurred in large slope areas, then mass movements accelerated their velocities | $r_u$ constant | $r_u$ constant | **(c)** |
| **Movement of Landslides** 1. Rapid motion At low residual strengths, landslides rapidly moved and reached the maximum velocities in the mid duration of the events. | $V_{max}$=42.8 | $V_{max}$=51.8 | **(d)** |
| 2. Deceleration and river damming After the whole slopes failed, motions were deaccelerated and soon ceased when the entire mass movements rushed to the opposite valley and dammed the river courses. | V=0.0 m/s | V=0.0 m/s | **(e)** |
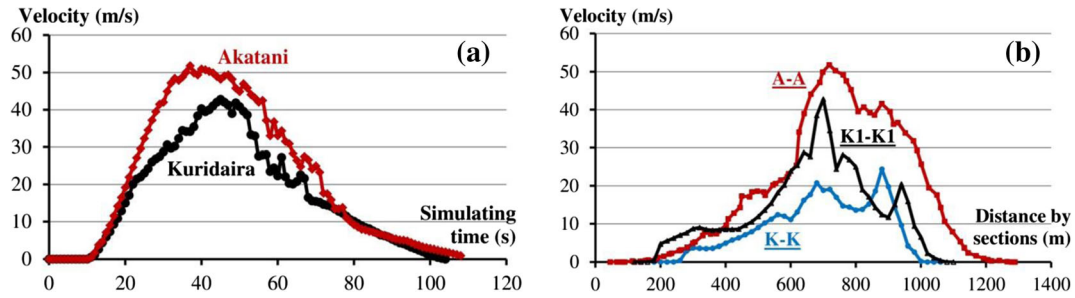
**Fig. 15** Velocities of the two landslides obtained via LS-RAPID modeling: **a** velocity vs. time and **b** velocity vs. distance along cross-sections of the Akatani slope (A-A) and the Kuridaira slope (K-K, K1-K1) measured from the head to the toe

obstacles of the opposite slopes to the downward movement of the landslides. The rapid landslides favor dam formation at the rivers before debris materials could be eroded and washed away. The simulation results indicate that the landslide mobility is an important factor contributing to the dam formation. Furthermore, the narrow V-shaped valleys allow the creation of high dams because of the small area in which the landslide masses could spread out. The contributing factors for dam formation agreed strongly with those described by Costa and Schuster (1987). In the formation process of the landslide dams at both sites, the sliding masses move downward the valleys, then collide straight into the opposite wall. The materials of the sliding masses then begin accumulating on the river bed. Due to an obstruction of the opposite wall in the narrow valleys, the debris spread out widely in both the upstream and downstream areas, generating a high run-up at the opposite banks. The landslide materials raise the river bed, and this accumulation body hinders the downslope movement of the progressive failures. The subsequent mass movement then slides along debris layers, hence failing to reach to the opposite bank. It then lays on the dam. A bulge in the middle of the cross-sections of both landslides is characterized by this motion process (Fig. 16). In addition, the wide-spreading motion of landslides forms debris fans in downstream accumulation areas. The model results suggest that the shape of the accumulation bodies are a result of the geometry of the river valleys. The results from the computer simulation further show that the critical pore pressure ratio triggering the Akatani landslide ($r_u = 0.36$) is higher than that for the Kuridaira landslide ($r_u = 0.33$). According to the recorded data, the

Akatani landslide took place after the Kuridaira landslide by several hours. This finding seems reasonable and fits into the sliding sequence of the two landslides triggered by continuous rainfall during Typhoon Talas. Since no groundwater data was recorded before the failures, it remains a question to what extent rainfall could have triggered the landslides. The role precipitation plays in triggering the landslides also remains unclear because of the strong influence of the deep-seated landslides on the strata of original slopes. In the computer model, however, the cumulative effect of rainfall on the saturation of slope materials is simply estimated via pore water pressure generation rate ($B_{ss}$) which indicates the potential to generate excess pore water pressure. The upper part of the slopes would then be unlikely to have been saturated because they are close to the ridge. The middle slope is likely to have been more saturated while the lower part might be well saturated. Therefore, $B_{ss} = 0.25–0.8$ and $B_{ss} = 0.25–0.85$ are, respectively, assigned to the Kuridaira and Akatani areas; a higher value is employed for a much more saturated zone. In addition, the effect of accumulative precipitation triggering the landslides is indirectly determined via pore pressure ratio ($r_u$) measured in the ring shear tests. A good result of the simulation model suggests an accurate measurement of pore pressure ratio ($r_u$) and a reasonable estimation of pore pressure generation rata ($B_{ss}$).

Moreover, the study findings contribute to the understanding of the failure characteristics of mudstone and shale slopes that are widely distributed globally, especially since the landslide mechanism by ring-shear apparatus has not been fully described as yet. Specifically, the exposed sliding surface of the Kuridaira landslide
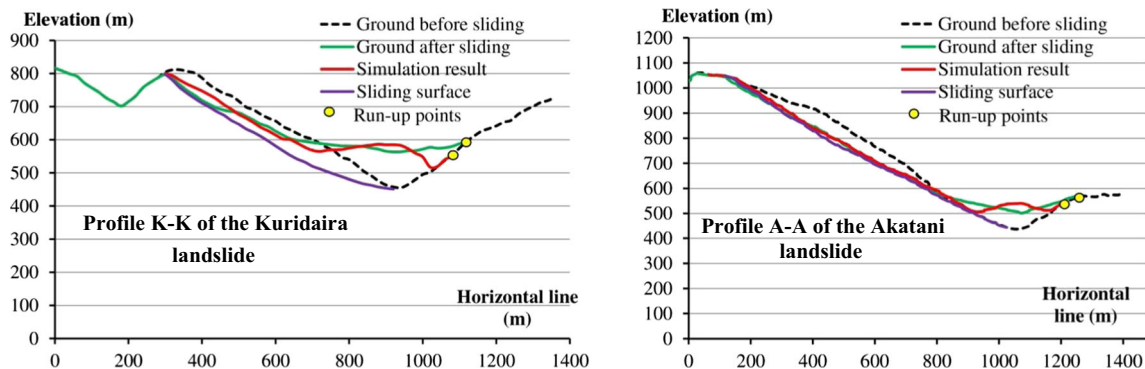


**Fig. 16** Comparison of ground surface after (m) sliding in 2011 and its elevation drawn from the simulation result

**Fig. 17** Sliding surface liquefaction behavior of shale samples under different normal stresses in ring shear tests

consists of weathered, fractured shale rocks, which are permeable, brittle, and coarse-grained materials. This geological feature is the most important factor contributing to the development of landslides, from gravitational slope deformation to the massive movement. On the other hand, in interbedded sandstone and mudstone zones, such as in the Akatani landslide, the potential sliding surface might be formed in the layer of sandstone-rich materials due to crushable materials and vulnerability to sliding surface liquefaction behavior.

## Conclusions

This paper presents the entire formation process of two massive dams formed by the two largest deep-seated landslides due to heavy rainfall during Typhoon Talas in the Kuridaira and Akatani valleys. The landslide dams are created on the tributary rivers of narrow, steep V-shaped valleys, which are significantly affected by extreme monsoon rainfall and specific geological features, namely broken formation, fractured discontinuities, and interbedded rocks of mudstone, sandstone, and shale. As indicated by the ring-shear tests, the slope movements result from excess pore water pressure generation under a small shear displacement of 2–7 mm or under an increase of pore water pressure with a critical ratio due to rainfall of 0.33–0.37. The deep-seated rapid landslides are thus attributed to the high mobility of samples K2 and A1 due to sliding surface liquefaction behavior. In addition to geomorphic features, landslide mobility is one of the main contributing factors to the dam formation. The entire formation process of the two landslide dams is examined by a computer simulation model that integrated physical soil parameters measured in the ring-shear tests. The evolution of landslide-formed dams—from local failures to massive movement across the entire slope, and through the accelerating failures and progressive motions to the complete damming of the rivers at the end of the motion—is described in detail. The simulation results are well examined to be consistent with the observed geomorphic evidences on the sites and recorded data. The finding regarding landslide mobility is crucial for future hazard assessment and disaster preparedness. The model is useful for estimating landslide parameters (such as depth, volume, velocity, and extent of the mass movement) and forecasting the potential of river damming in valleys surrounding the study area. By ascertaining the failure mechanism and predicting landslide behaviors and the dam formation, this research has practical significance in proactively establishing prevention and mitigation measures against potential deep-seated landslides and their secondary hazards on slopes that are similar to those in the Kuridaira and Akatani valleys in terms of geology and morphology.

## References

Bhandary NP, Yatabe R (2007) Ring shear tests on clays of fracture zone landslides and clay mineralogical aspects. In: Sassa K, Fukuoka H, Wang F, Wang G (eds) Progress in landslide science. Springer, Berlin, Heidelberg, pp 183–192

Chen C-Y and Chang J-M (2016) landslide dam formation susceptibility analysis based on geomorphic features. Landslides 13:1019–1033

Chigira M (2011) Geological and Geomorphological Characteristics of Deep-seated Catastrophic Landslides Induced by Rain and Earthquakes. J Chin Soil Water Conserv 42(4):265–278

Chigira M (2014) Geological and geomorphological features of deep-seated catastrophic landslides in tectonically active regions of Asia and implications for hazard mapping. Episodes 37(4):284–294 December 2014

Chigira M (2015) Geohazards in Asian countries. Proceedings of the 10th IAEG Asian regional conference, Kyoto, Japan, 26–29 Sept. Keynote paper, 7 pages

Chigira M, Tsou C-Y, Matsushi Y, Hiraishi N, Matsuzawa M (2013) Topographic precursors and geological structures of deep-seated catastrophic landslides caused by typhoon Talas. Geomorphology 201:479–493

Chigira M, Kanaori Y, Wakizaka Y, Yoshida H, Miyata Y (2016) Engineering geology. In: Moreno T, Wallis S, Kojima T, Gibbons W (eds) The geology of Japan. The Geological Society, London, pp 457–484

Costa, J.E. and Schuster, R.L. (1987): The formation and failure of natural dams, US Geological Survey, Open-File Report, pp. 87–392

Dunning SA, Mitchell WA, Rosser NJ, Petley DN (2007) The Hattian Bala rock avalanche and associated landslides triggered by the Kashmir earth quake of 8 October 2005. Eng Geol 93:130–144

Ermini L, Casagli N (2003) Prediction of the behaviour of landslide dams using a geomorphological dimensionless index. Earth Surf Process Landf 28:31–47

Ermini L, Casagli N, Farina P (2006) Landslide dams: analysis of case histories and new perspectives from the application of remote sensing monitoring techniques to hazard and risk assessment. Ital J Eng Geol Environ Special Issue 1:45–52

Evans SG (2006) The formation and failure of landslide dams: an approach to risk assessment. Ital J Eng Geol Environ. Special Issue 1. https://doi.org/10.4408/IJEGE.2006-01.S-02

Fan X, Tang CX, van Westen CJ, Alkema D (2012) Simulating dam-breach flood scenarios of the Tangjiashan landslide dam induced by the Wenchuan earthquake. Nat Hazards Earth Syst Sci 12:3031–3044

Fukuoka H, Sassa K, Wang G, Sasaki R (2006) Observation of shear zone development in ring-shear apparatus with a transparent shear box. Landslides 3:239–251

Fukuoka H, Sassa K, Wang G (2007) Shear behavior and shear zone structure of granular materials in naturally drained ring shear tests. In: Sassa K, Fukuoka H, Wang F, Wang G (eds) Progress in landslide science. Springer, Berlin, Heidelberg

Geertsema M, Clague JJ, Schwab J, Evans SG (2006) An overview of recent large catastrophic landslides in northern British Columbia, Canada. Eng Geol 83:120–143

GSI (2011) 10m-DEM data of the Kii peninsula. The Geospatial Information Authority of Japan. http://fgd.gsi.go.jp/download/menu.php

GSJ (1998) Geological map of the Kii peninsula (1:200,000). Seamless Digital Geological Map of Japan, Geological Survey of Japan, 1998. https://gbank.gsj.jp/geonavi/

Hayashi S, Uchida T, Okamoto A, Ishizuka T, Yamakoshi T, Morita K (2013) Countermeasures against landslide dams caused by Typhoon talas 2011. Asia-Pacific Tech Monitor 30(1, Jan-Mar 2013):20–26

Huang R, Pei X, Fan X, Zhang W, Li S, Li B (2012) The characteristics and failure mechanism of the largest landslide triggered by the Wenchuan earthquake, may 12, 2008, China. Landslides 9:131–142

JMA (2011) Hourly rainfall data at Kitayama Station. Japan meteorological agency. http://www.data.jma.go.jp/gmd/risk/obsdl/index.php

Kilburn CRJ, Petley DN (2003) Forecasting giant, catastrophic slope collapse: lessons from Vajont, northern Italy. Geomorphology 54:21–32

Kojima S, Nagata H, Yamashiroya S, Iwamoto N, Ohtan T (2015) Large deep-seated landslides controlled by geologic structures: prehistoric and modern examples in a Jurassic subduction–accretion complex on the Kii Peninsula, central Japan. Eng Geol 186:44–56

Korup O (2002) Recent research on landslide dams – a literature review with special attention to New Zealand. Prog Phys Geogr 26(2):206–235

Korup O (2005) Geomorphic hazard assessment of landslide dams in South Westland, New Zealand: fundamental problems and approaches. Geomorphology 66:167–188

Miyagi T, Yamashina S, Esaka F, Abe S (2011) Massive landslide triggered by 2008 Iwate-Miyagi inland earthquake in the Aratozawa dam area, Tohoku, Japan. Landslides 8:99–108

MOI (2014) Report on jure landslide, Mankha VDC, Sindhupalchowk District, Nepal government Ministry of Irrigation, august 24, 2014, 29 pages in English

Peng M, Zhang L-M (2012) Breaching parameters of landslide dams. Landslides 9(1):13–31

Petley DN, Allison RJ, (1997) The mechanics of deep-seated landslides. Earth Surf Process Landf 22(8):747–758

SABO (2013) A pamphlet released in October, 2013 on Overview of the 2011 disaster induced by Typhoon No. 12, Implementation of an urgent investigation and countermeasures to disaster areas. The Kii Mountain District SABO Office, Kinki Regional Development Bureau. The Ministry of Land, Infrastructure, Transport and Tourism. http://www.kkr.mlit.go.jp/kiisanchi/outline/, 24 pages (in Japanese)

SABO (2014a) A PDF document dated in July, 2014 on Deep-seated landslides occurred during Typhoon No.12 in September 2011 in Kuridaira area. The Kii Mountain District SABO Office, Kinki Regional Development Bureau. The Ministry of Land, Infrastructure, Transport and Tourism, 8 pages (in Japanese)

SABO (2014b) A PDF document dated in July, 2014 on Deep-seated landslides occurred during Typhoon No.12 in September 2011 in Akatani area. Kii Mountain District SABO Office, Kinki Regional Development Bureau. The Ministry of Land, Infrastructure, Transport and Tourism, 23 pages (in Japanese)

SABO (2015) DEM data and reports on the investigation of the 2011 landslide disasters offered by the Kii Mountain District SABO Office

Sassa K (1996) Prediction of earthquake induced landslides. Proceedings of 7th International Symposium on Landslides, AA Balkema, Trondheim, Vol. 1, pp. 115–132

Sassa K (2005) Landslide disasters triggered by the 2004 mid-Niigata prefecture earthquake in Japan. Landslides 2:135–142

Sassa K, Fukuoka H, Wang G, Ishikawa N (2004) Undrained dynamic-loading ring-shear apparatus and its application to landslide dynamics. Landslides 1(1):7–19

Sassa K, Nagai O, Solidum R, Yamazaki Y, Ohta H (2010) An integrated model simulating the initiation and motion of earthquake and rain induced rapid landslides and its application to the 2006 Leyte landslide. Landslides 7(3):219–236

Sassa K, Dang K, He B, Takara K, Inoue K, Nagai O (2014) A new high-stress undrained ring-shear apparatus and its application to the 1792 Unzen-Mayuyama megaslide in Japan. Landslides 11(5):827–842

Setiawan H (2017) Landslide hazard assessment on the upstream of dam reservoir. PhD thesis. Kyoto university

Stefanelli C. T, Segoni S, Casagli N and Catani F (2017) Assessing landslide dams evolution: a methodology review. Advancing culture of living with Landslides, pp. 253–258

Tien P. V, Sassa K, Takara K, Dang K, Luong LH and Ha ND (2017) Simulating the formation process of the Akatani landslide dam induced by rainfalls in Kii peninsula, Japan. Advancing culture of living with Landslides, pp. 497–506

Tien P. V, Sassa K, Takara K, Fukuoka H, Khang D, Shibasaki T, Hendy S, Ha N. D and Luong L. H (2018) Mechanism of large-scale deep-seated landslides induced by rainfall in gravitationally deformed slopes: a case study of the Kuridaira landslide in Kii peninsula. Landslide dynamics: ISDR-ICL landslide interactive teaching tools, springer international publishing, doi:https://doi.org/10.1007/978-3-319-57777-7_52

Tsou C-Y, Feng Z-Y, Chigira M (2011) Catastrophic landslide induced by Typhoon Morakot, Shiaolin, Taiwan. Geomorphology 127(3–4):166–178

Wang F, Hayashi H, Okeke AC, Mitani Y, Yang H, Kuwada Y, Baba S (2014) Using microtremor Array survey to evaluate the possibility of piping-induced landslide dam failure. Landslide Sci Safer Geoenvironment 3:649–657

Yamada M, Matsushi Y, Chigira M, Mori J (2012) Seismic recordings of landslides caused by typhoon Talas (2011), Japan. Geophys Res Lett 39:L13301

**P. Van Tien** (✉) · **K. Takara** · **N. D. Ha** · **H. Setiawan**
Disaster Prevention Research Institute,
Kyoto University,
Kyoto, Japan
Email: phamtiengtvt@gmail.com

**P. Van Tien** · **D. H. Loi**
Institute of Transport Science and Technology,
1252 Lang Street, Dong Da, Hanoi, Vietnam

**K. Sassa** · **K. Dang**
International Consortium on Landslides,
Kyoto, Japan

**H. Fukuoka**
Research Institute for Natural Hazards and Disaster Recovery,
Niigata University,
Niigata, Japan

**K. Dang**
VNU University of Science,
Hanoi, Vietnam

**T. Shibasaki**
Japan Conservation Engineers & CO., LTD.,
Tokyo, Japan